






Epitaxial growth of hexagonal BaNiO_{3-δ} thin films on SrTiO₃ (111) substratesBinod Paudel ¹, Krishna P. Koirala,¹ Le Wang ^{1,*}, Zengqing Zhuo,² Mark E. Bowden,¹ Peter V. Sushko ¹, Wanli Yang,² George E. Sterbinsky ³, Scott A. Chambers,¹ Tiffany C. Kaspar,^{1,†} and Yingge Du ¹¹Physical and Computational Sciences Directorate, Pacific Northwest National Laboratory, Richland, Washington 99354, USA²Advanced Light Source, Lawrence Berkeley National Laboratory, Berkeley, California 94720, USA³Advanced Photon Source, Argonne National Laboratory, Lemont, Illinois 60439, USA

(Received 17 May 2023; accepted 8 August 2023; published 28 August 2023)

Transition metal oxides containing nickel species in oxidation states higher than 3+ often exhibit high catalytic activity, which makes them promising for applications as advanced electrocatalysts for water splitting and fuel cells. Here, we examine the structure and properties of BaNiO₃ (BNO) thin films, containing formally Ni⁴⁺, grown on SrTiO₃ (111) substrates using oxygen-plasma-assisted molecular beam epitaxy. X-ray diffraction and scanning transmission electron microscopy measurements reveal that BNO films have a hexagonal structure with *c*- and *a*-axes of mixed textures showing epitaxial relationships BNO (0001) || SrTiO₃ (111) and BNO (10 $\bar{1}$ 0) || SrTiO₃ (111), respectively. The formation of the *a*-axis texture is dominant due to the smaller lattice mismatch with the substrate. Density functional theory calculations confirm that the hexagonal BNO film with the *a*-axis texture is energetically more favorable than the competing *c*-axis texture. Detailed spectroscopy data analysis indicates that hexagonal BNO films contain mixtures of Ni²⁺, Ni³⁺, and Ni⁴⁺ species, with Ni⁴⁺ being dominant. Our study provides insights into stabilizing Ni⁴⁺ in complex oxides, which is important for further exploration of the potential of materials containing Ni⁴⁺.

DOI: [10.1103/PhysRevMaterials.7.085004](https://doi.org/10.1103/PhysRevMaterials.7.085004)

I. INTRODUCTION

ABO₃-type perovskite rare earth nickelates RNiO₃ (where *R* denotes lanthanide) are an extensively investigated family of complex oxides due to their rich phase diagrams [1–3]. This oxide family demonstrates exotic physical properties, such as metal-insulator transitions [4], charge ordering [5], unusual magnetic ordering [6], and colossal resistive switching [7,8]. Integration of nickelates into heterostructures through thin film epitaxy can induce orbital degeneracy breaking and quantum confinement effects that effectively modulate their functional properties [2,9,10]. The sensitivity of nickelates to the details of the structure and composition is made evident by the fact that superconductivity was only observed in the reduced R_{1-x}Sr_xNiO₂ and R_{1-x}Ca_xNiO₂ epitaxial thin films [11–14], whereas it is absent in the bulk R_{1-x}Sr_xNiO₂ [15,16].

Recently, nickelates have also garnered special attention in catalysis because of their excellent electrocatalytic performance [17–20], which can be attributed to the small or negative charge transfer energy (Δ) defined as the difference between the nickel 3*d*-band and the oxygen 2*p*-band edge (negative Δ corresponds to the nickel 3*d*-band below the oxygen 2*p*-band maximum) that results in strong nickel 3*d*-oxygen 2*p* hybridization [21]. Hole doping in RNiO₃ can push the nickel formal valence above 3+ [22], which can further increase the extent of nickel 3*d*-oxygen 2*p* hybridization [19], thereby promoting an enhancement in the

electrocatalytic activity [18,20]. However, it has been shown that the synthesis of parent perovskite phases R_{1-x}Sr_xNiO₃ and R_{1-x}Ca_xNiO₃ in the form of thin films is challenging due to the instability of the high-valence nickel species [22–25]. Phase segregation was observed when attempting to deposit SrNiO_{3-δ} (SNO) on (001)-oriented perovskite-like single-crystal substrates using oxygen-plasma-assisted molecular beam epitaxy (OPA-MBE) [26,27]. Two coexisting oxygen-deficient Ruddlesden-Popper phases, Sr₂NiO₃ and SrNi₂O₃, formed instead, and nickel ions were stabilized in the energetically preferred Ni²⁺ state [26]. Previous studies reported the formation of single unit cell (u.c.) SNO in superlattices with LaFeO₃ and SrTiO₃ (STO) [27,28]. However, the instability of SNO in the top layer of these superlattices limits exploration of the impact of Ni⁴⁺ on the mechanisms and characteristics of electrocatalytic reactions that occur primarily at the surface.

Bulk SNO is expected to form a hexagonal structure with a face-shared arrangement of NiO₆ octahedra because its tolerance factor (*t*) is larger than unity [29]. Due to the high Gibbs formation energy of Ni⁴⁺ [30], there has been very limited success in the synthesis of bulk hexagonal-structured SNO until recently [31,32]. Replacement of strontium with larger size barium can stabilize hexagonal closest packing [32]. Thus, bulk hexagonal-structured BaNiO₃ (BNO) has been successfully synthesized by several groups [18,33–38]. However, we are not aware of reports on synthesis of BNO epitaxial thin films.

Here, we examined the structural and electronic properties of BNO thin films synthesized by OPA-MBE. We observed that hexagonal-phase BNO thin films with *c*-axis and *a*-axis mixed textures are stabilized on STO (111) substrates. We

*Corresponding author: le.wang@pnl.gov†Corresponding author: tiffany.kaspar@pnl.gov

used density functional theory (DFT) simulations to evaluate the phase stability of BNO thin films on (111) oriented perovskite single crystal substrates. We found that hexagonal BNO thin films are energetically more stable than those in the cubic perovskite phase when deposited on substrates with lattice parameters ranging from 3.8 to 4.1 Å. The a -axis texture, BNO (10 $\bar{1}$ 0)/STO (111), is energetically more favorable due to the smaller lattice mismatch with the substrate compared to the c -axis texture, BNO (0001)/STO (111). X-ray photoelectron spectroscopy (XPS) and X-ray absorption spectroscopy (XAS) measurements revealed that BNO films contain nickel species with valences of Ni²⁺, Ni³⁺, and Ni⁴⁺, with Ni⁴⁺ being dominant.

II. RESULTS AND DISCUSSION

To prepare the STO substrate, we employed a wet etching method similar to that described elsewhere [39]. BNO films were grown on STO (111) substrates by OPA-MBE. Barium and nickel were evaporated from effusion cells, and their evaporation rates were calibrated using a quartz crystal microbalance prior to growth. The substrate temperature was maintained at 650 °C, and the activated oxygen partial pressure was kept at $\sim 5 \times 10^{-6}$ Torr throughout the growth process. To prevent the oxygen vacancy formation in BNO films, an alternating deposition and annealing approach was employed, as described in our previous work [23]. *In situ* reflection high-energy electron diffraction (RHEED) was used to monitor the overall growth process, as shown in Supplemental Material Fig. S1 [40]. After growth, the samples were gradually cooled in an activated oxygen atmosphere at a chamber pressure of $\sim 2 \times 10^{-5}$ Torr. The temperature was ramped down from 650 to 500 °C at a rate of 25 °C/min, followed by a 1 hour annealing step at 500 °C. Subsequently, a second ramp was performed from 500 to 250 °C at a rate of 5 °C/min, followed by a 2 hours annealing step at 250 °C. Finally, the samples were cooled to room temperature at a rate of 1 °C/min [41,42]. High-resolution out-of-plane X-ray diffraction (XRD) $\theta-2\theta$ scan [Fig. 1(a)] reveals two well-defined families of peaks ($h0\bar{h}0$, $h = 1, 2, 3, 4$) and ($000l$, $l = 2, 4$), indicating that the BNO film nucleates with both a -axis and c -axis textures. The simulations (see Supplemental Material Fig. S2 [40]) clearly show the overlap of the (20 $\bar{2}$ 0) and (40 $\bar{4}$ 0) a -axis peaks with the (0002) and (0004) c -axis peaks, respectively. To examine the film's symmetry and epitaxial relationships, two off-axis phi scans were performed along the film (22 $\bar{4}$ 0) and (10 $\bar{1}$ 3) reflections, and along the substrate (112) reflection, as shown in Fig. 1(b). The STO (112) phi scan shows three peaks separated by 120°, corresponding to the threefold triangular surface symmetry of the STO (111) substrate. A phi scan was performed to probe the in-plane orientation of the c -axis texture by measuring the BNO (10 $\bar{1}$ 3) reflection at an appropriate χ angle. The alignment between the six BNO features and the three STO peaks confirms the sixfold rotational symmetry of hexagonal c -axis BNO, which directly grows on the in-plane triangular STO (111) surface with an epitaxial relationship of BNO (0001) [10 $\bar{1}$ 0] || STO (111) [11 $\bar{2}$]. Likewise, the in-plane orientation of the a -axis texture was determined with a phi scan of the BNO (22 $\bar{4}$ 0) reflection at an appropriate χ angle, which reveals the epitaxial relationship BNO (10 $\bar{1}$ 0) [0001] || STO (111) [11 $\bar{2}$].

The 30° offset between the two BNO phi scans is a consequence of the observed epitaxial relationships and the selection of particular reflections for the phi scans. The six observed BNO peaks indicate the overall sixfold rotational symmetry of the a -axis texture, which arises from the three in-plane tetragonal BNO domains rotated by 120°, as depicted in Supplemental Material Fig. S3(a) [40]. Reciprocal space mapping (RSM) (Supplemental Material Fig. S3(c) [40]) reveals that the BNO film was partially relaxed.

Additional structural information on the BNO film was obtained using high-angle annular dark field-scanning transmission electron microscopy (HAADF-STEM). Figure 1(c) shows an atomic-resolution HAADF-STEM image of the BNO/STO heterostructure viewed along the STO $\langle 11\bar{2} \rangle$ direction. An interfacial transition region (marked by an arrow and extensively described in Supplemental Material Fig. S4 [40]) was observed at the BNO/STO interface. Beyond the interfacial transition region, the a -axis texture of hexagonal-phase BNO [see the schematic in Fig. 1(d)] was clearly observed in the left side of the STEM image, as confirmed by the fast Fourier transform (FFT) patterns [Fig. 1(e)]. In addition, we observed a lattice structure with a slightly different appearance on the right side of the STEM image (marked by a yellow rectangle). FFT patterns [Fig. 1(f)] in this region perfectly match those [Fig. 1(e)] on the left side of the STEM image, suggesting that it is not related to the c -axis texture, but to be the a -axis texture. To validate our findings further, we rotated the simulated STEM-HAADF image of the a -axis texture by up to 2° (Supplemental Material Fig. S5 [40]), and the results showed a strong correspondence with the STEM-HAADF image. The distortions on the hexagonal lattice are likely due to the compressive and tensile strains along the in-plane and out-of-plane directions, respectively. The c -axis texture detected in the XRD experiments was not observed in the HAADF-STEM images. To verify its presence, we performed a phi scan for a peak inclined to the (0001) planes and found it at the anticipated d -spacing and inclination angle [Fig. 1(b)]. Since the (000 l) and ($h0\bar{h}0$) peaks locate closely when $l = h$, resolution of the out-of-plane $\theta-2\theta$ scan is not sufficient to estimate the volume fractions corresponding to these different orientations. However, at high diffraction angles where the peaks are better resolved, it appears that the (0001) orientation is considerably less abundant. Consequently, the probability of lifting out a region of (0001)-oriented BNO for STEM imaging is quite low and we identified only ($h0\bar{h}0$) orientation in the focused ion beam sections we imaged.

In order to understand why both the a -axis and c -axis textures were formed during hexagonal (h)-BNO growth, we examined the dependence of their potential energies on the strain imposed by a cubic perovskite lattice terminated with a (111) plane. In both cases, we varied the perovskite lattice constant and recalculated the in-plane vectors of the supercells representing the textures of the a - and c -axes accordingly. The internal atomic coordinates and the supercell vectors in the out-of-plane direction were fully relaxed. Similar calculations were performed for the perovskite BNO simulated as a continuation of the STO (111) substrate. The supercells for strained perovskite and hexagonal BNO on STO(111) are shown in

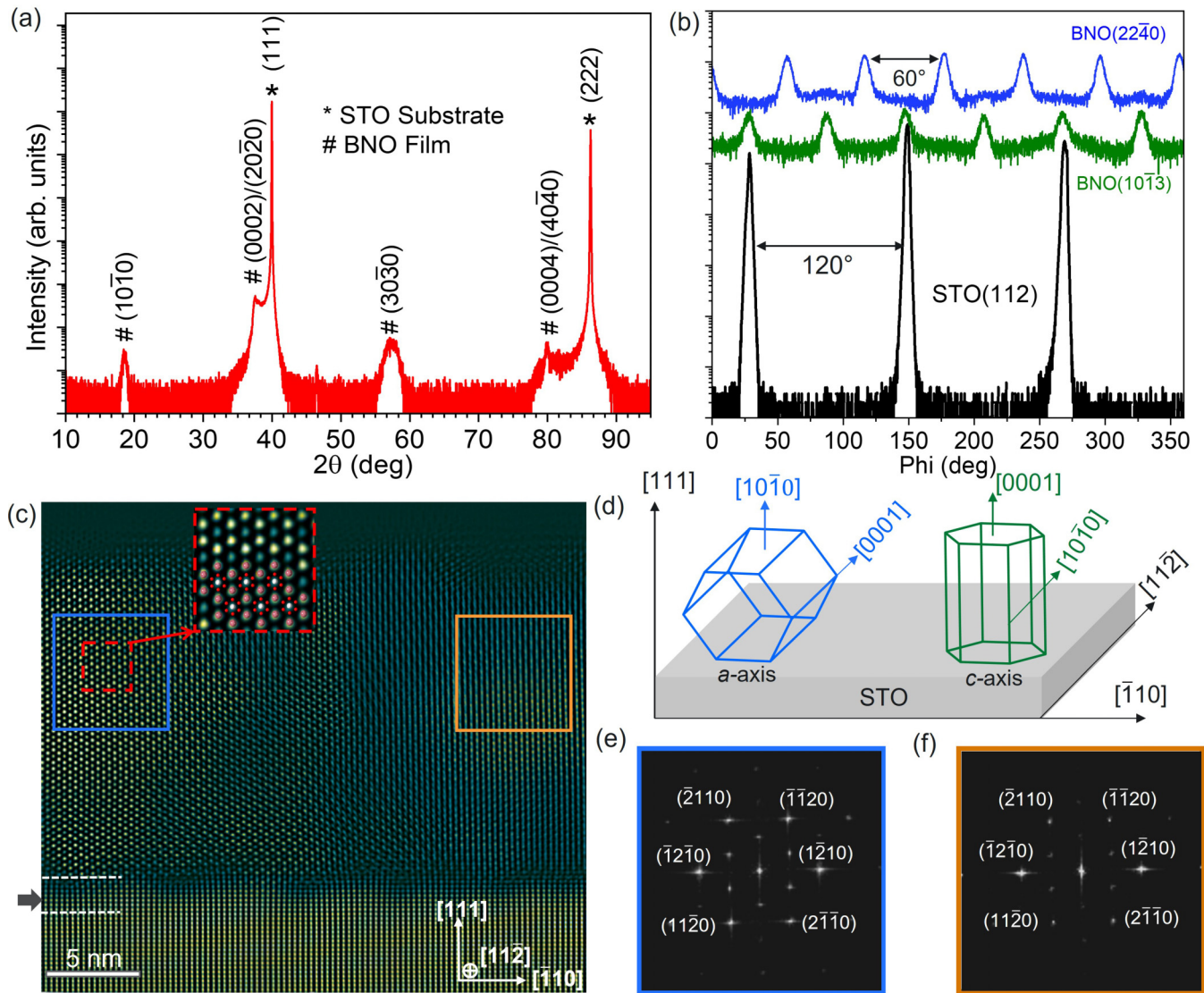


FIG. 1. Synthesis of epitaxial hexagonal BNO film on STO (111) and structural characterization. (a) High-resolution XRD θ - 2θ scan showing the presence of mixed textures of the a - and c -axes. (b) Phi scans along two different planes demonstrating two distinct epitaxial relationships. (c) STEM-HAADF image viewed along the STO $\langle 11\bar{2} \rangle$ zone axis, highlighting two “different” lattice structures in the selected regions. The hexagonal structure of BNO (pink spheres, barium; white spheres, nickel; red spheres, oxygen) is overlaid for comparison. The black arrow denotes the interfacial transition layer. (d) Schematics illustrating the epitaxial relationships of the two textures on STO (111). (e) and (f) Fast Fourier transforms of the two selected regions in (c), revealing the corresponding reciprocal space information.

Supplemental Material Fig. S6 [40]. Figure 2 shows the crystal structure orientations of the a -axis and c -axis textures as viewed along the STO $\langle 111 \rangle$ direction and strain energy comparisons among the two h-BNO textures and perovskite BNO. The c -axis texture is under an identical compressive biaxial lattice mismatch of $\sim 1.93\%$ in both in-plane directions along BNO $[11\bar{2}0] \parallel \text{STO} [\bar{1}10]$ and BNO $[10\bar{1}0] \parallel \text{STO} [11\bar{2}]$, as shown in Fig. 2(a). On the other hand, compressive mismatches of $\sim 1.93\%$ and $\sim 0.52\%$ are present along the BNO $[11\bar{2}0] \parallel \text{STO} [\bar{1}10]$ and BNO $[0001] \parallel \text{STO}[11\bar{2}]$ directions, respectively, for the a -axis texture [Fig. 2(b)]. The smaller lattice mismatch in the a -axis texture along BNO $[0001] \parallel \text{STO} [11\bar{2}]$ is observed due to a coincidence lattice match with the 30° -rotated STO (111) in-plane lattice constant, i.e., $\sqrt{6}a_{\text{STO}}$ ($a_{\text{STO}} = 3.905 \text{ \AA}$, $\sqrt{6}a_{\text{STO}} = 9.57 \text{ \AA}$) with

$2c_{\text{BNO}}$ ($c_{\text{BNO}} = 4.81 \text{ \AA}$, $2c_{\text{BNO}} = 9.62 \text{ \AA}$). The calculated energy minimum for the a -axis texture falls at a smaller lattice constant than that of the c -axis texture due to their unique strains, as shown in Fig. 2(c). The a -axis texture has its minimum energy at $a_{\text{Sub}} = 5.57 \text{ \AA}$, while the c -axis texture has an energy minimum when a_{Sub} equals the bulk lattice parameter of BNO, i.e., 5.63 \AA . For the STO (111) substrates, the strain energy associated with a -axis-textured BNO is 25 meV lower per formula unit (f.u.) than for its c -axis counterpart, indicating that the a -axis texture is the most energetically favorable configuration. For comparison, the perovskite BNO (111)/STO (111) configuration is significantly less stable (by $\sim 1.3 \text{ eV}$ per f.u.) than either c -axis or a -axis textures, indicating that perovskite BNO is unlikely to nucleate. These calculations are consistent with experimental observations of

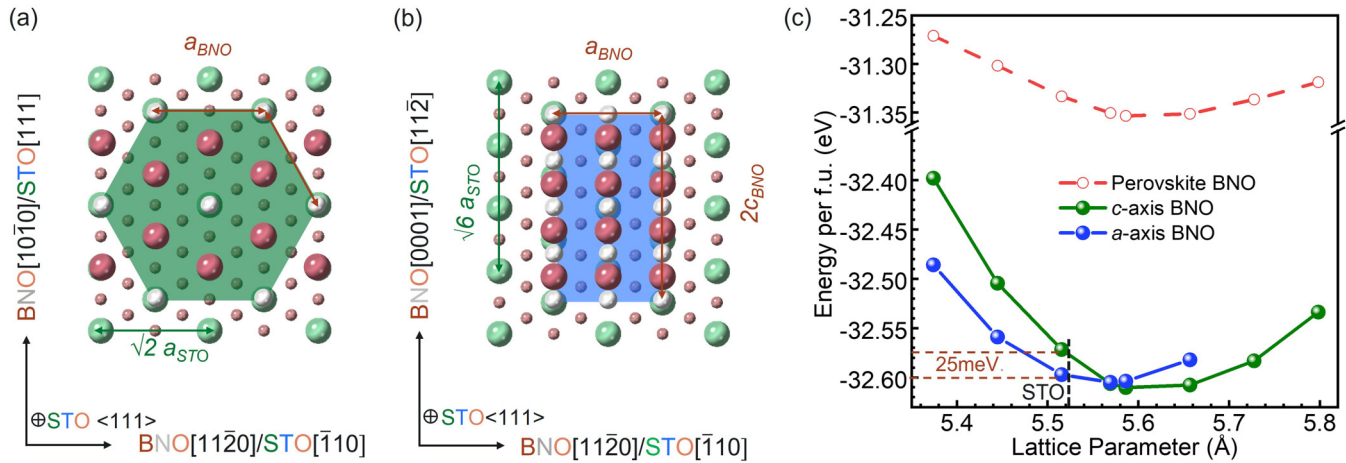


FIG. 2. Crystal structures and corresponding BNO potential energy for the film/substrate orientations for two h-BNO textures viewed down the STO $\langle 111 \rangle$ zone axis. (a) Crystal structure of the c -axis texture with an epitaxial relationship of BNO (0001) $[10\bar{1}0] \parallel \text{STO} (111) [11\bar{2}]$ and (b) a -axis texture with an epitaxial relationship of BNO (10 $\bar{1}0$) $[0001] \parallel \text{STO} (11\bar{2}) [111]$. (c) Energy per formula unit versus substrate lattice parameter for the two textures of h-BNO and the perovskite BNO phase supported on cubic substrates.

mixed textures in the h-BNO film. This coexistence of the two phases is attributed to the small difference in their stability at the epitaxial strains imposed by the STO (111) substrate. In addition, based on our DFT simulations [Fig. 2(c)], both textures are sensitive to strain, which therefore can be utilized to favor preferential formation of one texture over another. While the potential energy minima for these textures are relatively close to each other, the quadratic dependence of the potential energy on the lattice parameter ensures that the energy difference between these phases increases at least linearly with increasing tensile or compressive strain. Specifically, for the LaAlO_3 substrate (lattice parameter, $\sim 3.86 \text{ \AA}$), the energy difference between textures is expected to be three times larger than that found for the SrTiO_3 substrate, thus highly increasing the likelihood of achieving a single-phase a -axis texture of h-BNO film. Conversely, employing a single-crystal substrate with a large lattice constant, e.g., KTaO_3 (lattice parameter, $\sim 3.96 \text{ \AA}$), will switch the texture prevalence from the a -axis to the c -axis, even if marginally so.

To identify the nickel valence in BNO, we conducted *in situ* XPS along with *ex situ* L - and K -edge XAS measurements. The reference spectra for Ni^{3+} and Ni^{2+} were measured using an oxygen plasma annealed NdNiO_3 (NNO) film and a NiO film, respectively [26]. Nickel $2p$ and $3p$ XPS spectra are shifted so that the corresponding oxygen $1s$ peak falls at 530.0 eV. As shown in Fig. 3(a), the nickel $2p$ line shapes for BNO show a clear distinction from the Ni^{3+} and Ni^{2+} reference spectra. The nickel $2p_{3/2}$ main feature peak for BNO (marked by a red dashed line) is shifted to a higher binding energy relative to that of NNO, suggesting that the nickel valence in BNO should be higher than $3+$. Based on the chemical shift ($\sim 2 \text{ eV}$) of the nickel $2p_{3/2}$ peak relative to the nickel $2p$ peak of NNO, we speculate that the nickel valence in BNO is dominated by Ni^{4+} . Additionally, a shoulder located at the lower binding energy side is also observed in the nickel $2p_{3/2}$ feature for BNO, indicating the presence of mixed nickel valence in BNO. The nickel $2p_{3/2}$ shoulder feature peak energy is the same as that of NNO, suggesting that the nickel

valence in BNO includes Ni^{3+} . The nickel valence assignment (a mixture of Ni^{4+} and Ni^{3+}) from nickel $2p$ XPS is consistent with nickel $3p$ XPS [Supplemental Material Fig. S7(a) [40]] and corroborated by XAS measurements collected at the nickel K -edge [Supplemental Material Fig. S7(b) [40]] and the nickel L -edge. Figure 3(b) shows the total electron yield (TEY) mode nickel L -edge spectra for BNO, along with that of the Ni^{3+} and Ni^{2+} references. The main feature peaks at the $L_{2,3}$ edges shift toward higher photon energy compared to the Ni^{3+} reference, indicating that the dominant formal nickel valence in BNO should be higher than Ni^{3+} . The measured energy shift ($\sim 1.5 \text{ eV}$) of the nickel L -edges relative to that in NNO suggests that the dominant nickel valence in BNO is Ni^{4+} [43], consistent with our XPS analysis. Moreover, the shoulders (observed at the lower photon energy side) of both the L_3 - and L_2 -edges match the peak positions of the Ni^{2+} and Ni^{3+} reference spectra, confirming the presence of a mix of Ni^{4+} , Ni^{3+} , and Ni^{2+} in BNO. In contrast to XPS, which mainly detects the near surface (the effective attenuation length of XPS is $\sim 5 \text{ nm}$) [44], XAS (the attenuation length of TEY mode is $> 10 \text{ nm}$) [45] can probe deeper. Thus, we conclude that the Ni^{2+} feature, observed in nickel L -edge XAS but mostly absent in nickel $2p$ XPS, could be ascribed to the contribution from the region close to the interface. This is confirmed by our STEM measurements (Supplemental Material Fig. S8 [40]), which capture NiO secondary phases close to the interfacial regions. The existence of the insulating NiO secondary phases in BNO films can strongly affect the in-plane electrical transport behavior. These secondary phases might be responsible for the observed insulating behavior manifested by a high resistivity of $2.1 \times 10^2 \Omega \text{ cm}$ at 300 K, as shown in Fig. 3(d). In contrast, NNO shows metallic behavior with a resistivity of only $\sim 3.2 \times 10^{-4} \Omega \text{ cm}$ at 300 K [26].

The valence states of transition metals (TMs) in oxides can also be qualitatively assessed by the pre-edge spectral feature at the oxygen K -edge. For the same TM, a lower oxygen K -pre-edge peak energy corresponds to a higher TM valence state [46]. Moreover, a higher intensity of the oxygen

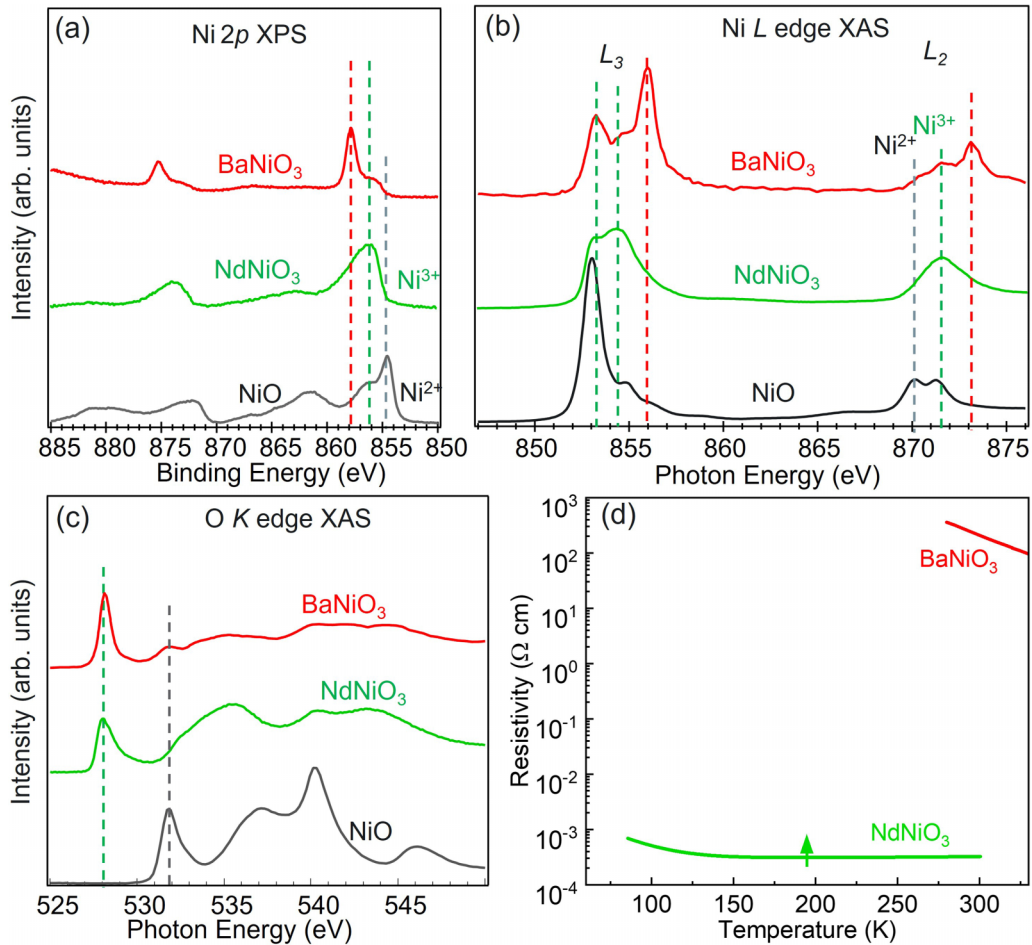


FIG. 3. Spectroscopy data and in-plane transport behavior. (a) *In situ* nickel $2p$ XPS. The nickel $2p_{2/3}$ peak position is marked by dashed lines. (b) Nickel L -edge XAS. The nickel L_2 -edge peak position for BNO, NdNiO₃, and NiO is marked by red, green, and gray dashed lines, respectively. (c) Oxygen K -edge XAS. The oxygen K -pre-edge position for NdNiO₃ and NiO is marked by green and gray dashed lines, respectively. (d) Temperature-dependent resistivity of BaNiO₃ and NdNiO₃. The green arrow denotes the metal-insulator transition temperature for NdNiO₃.

K -pre-edge peak suggests stronger TM $3d$ and oxygen $2p$ hybridization. We compared the oxygen K -pre-edge feature of BNO with the reference spectra of NNO and NiO. As shown in Fig. 3(c), the oxygen K -pre-edge feature peak of BNO falls at the same position (~ 528 eV) as that of NNO, suggesting that the nickel valence in BNO is close to Ni³⁺. Compared to NNO, the higher oxygen K -pre-edge peak intensity of BNO indicates stronger nickel $3d$ -oxygen $2p$ hybridization, which can be ascribed to the contribution from Ni⁴⁺ (we should note that the oxygen K -pre-edge feature peak position of Ni⁴⁺ is very close to that of Ni³⁺) [19,46]. Moreover, the coincidence of a small feature at ~ 532 eV with the oxygen K -pre-edge feature peak of NiO also implies the presence of Ni²⁺ in BNO, in agreement with the nickel L -edge XAS measurements.

III. SUMMARY

We have synthesized BNO thin films on (111)-oriented STO substrates by OPA-MBE. Our XRD and STEM studies demonstrate that BNO films can be stabilized in the hexagonal phase with a -axis and c -axis mixed textures, and thus display

epitaxial relationships of BNO (10 $\bar{1}$ 0) [0001] \parallel STO (111) [11 $\bar{2}$] and BNO (0001) [10 $\bar{1}$ 0] \parallel STO (111) [11 $\bar{2}$] for a -axis and c -axis texture, respectively. We found that the preferential formation of the a -axis texture is due to the smaller lattice mismatch with the STO substrate. Our DFT calculations confirm that the a -axis texture is energetically favorable over the competing c -axis texture and demonstrate that the a -axis texture prevalence stems from its better match to the in-plane lattice parameters of the STO substrate and, therefore, the lower energy penalty associated with the lattice mismatch. Spectroscopy data demonstrate that the nickel valence in BNO films is a mixture of Ni²⁺, Ni³⁺, and Ni⁴⁺ oxidation states, with Ni⁴⁺ being dominant. STEM measurements demonstrate that NiO secondary phase formation (which contributes to the Ni²⁺ feature) occurs close to the interface, and an interfacial transition region exists at the BNO/STO interface. Electron-energy-loss spectroscopy (EELS) measurements reveal the interfacial transition region is ~ 9 u.c. thick, and the composition changes from Sr_{1-x}Ba_xTiO₃ (close to the substrate) to BaTi_{1-y}Ni_yO₃ (close to the BNO film). These results highlight the possibility of stabilizing the Ni⁴⁺ valence state in thick

oxide thin films, which will offer a good platform to investigate the effects of a high nickel valence on electrocatalytic performance.

ACKNOWLEDGMENTS

This work was supported by the U.S. Department of Energy (DOE), Office of Science, Basic Energy Sciences, Division of Materials Sciences and Engineering, Synthesis and Processing Science Program under Award No. 10122. Nickel *L*-edge and oxygen *K*-edge XAS measurements were performed at the Advanced Light Source

of Lawrence Berkeley National Laboratory, which is supported by the Director, Office of Science, Office of Basic Energy Sciences, U.S. Department of Energy under Contract No. DE-AC02-05CH11231. Nickel *K*-edge XAS measurements were performed at the Advanced Photon Source, a U.S. DOE Office of Science User Facility operated by Argonne National Laboratory under Contract No. DE-AC02-06CH11357. This research used resources of the National Energy Research Scientific Computing Center—a DOE Office of Science User Facility supported by the Office of Science of the U.S. Department of Energy under Contract No. DE-AC02-05CH11231 using NERSC Award BES-ERCAP0024614.

-
- [1] G. Catalan, *Phase Transit.* **81**, 729 (2008).
- [2] S. Middey, J. Chakhalian, P. Mahadevan, J. W. Freeland, A. J. Millis, and D. D. Sarma, *Annu. Rev. Mater. Res.* **46**, 305 (2016).
- [3] V. Bisogni, S. Catalano, R. J. Green, M. Gibert, R. Scherwitzl, Y. Huang, V. N. Strocov, P. Zubko, S. Balandeh, J.- M. Triscone, G. Sawatzky, and T. Schmitt, *Nat. Commun.* **7**, 13017 (2016).
- [4] J. B. Torrance, P. Lacorre, A. I. Nazzal, E. I. Ansaldo, and C. Niedermayer, *Phys. Rev. B* **45**, 8209(R) (1992).
- [5] J. A. Alonso, J. L. García-Muñoz, M. T. Fernández-Díaz, M. A. G. Aranda, M. J. Martínez-Lope, and M. T. Casais, *Phys. Rev. Lett.* **82**, 3871 (1999).
- [6] J. L. García-Muñoz, J. Rodríguez-Carvajal, and P. Lacorre, *Europhys. Lett.* **20**, 241 (1992).
- [7] J. Shi, Y. Zhou, and S. Ramanathan, *Nat. Commun.* **5**, 4860 (2014).
- [8] L. Wang, S. Dash, L. Chang, L. You, Y. Feng, X. He, K. Jin, Y. Zhou, H. G. Ong, P. Ren, S. Wang, L. Chen, and J. Wang, *ACS Appl. Mater. Interfaces* **8**, 9769 (2016).
- [9] S. Catalano, M. Gibert, J. Fowlie, J. Íñiguez, J.- M. Triscone, and J. Kreisel, *Rep. Prog. Phys.* **81**, 046501 (2018).
- [10] G. A. Pan *et al.*, *Nat. Mater.* **21**, 160 (2022).
- [11] D. Li, K. Lee, B. Y. Wang, M. Osada, S. Crossley, H. R. Lee, Y. Cui, Y. Hikita, and H. Y. Hwang, *Nature (London)* **572**, 624 (2019).
- [12] M. Osada, B. Y. Wang, B. H. Goodge, K. Lee, H. Yoon, K. Sakuma, D. Li, M. Miura, L. F. Kourkoutis, and H. Y. Hwang, *Nano Lett.* **20**, 5735 (2020).
- [13] S. Zeng, C. Li, L. E. Chow, Y. Cao, Z. Zhang, C. S. Tang, X. Yin, Z. S. Lim, J. Hu, P. Yang, and A. Ariando, *Sci. Adv.* **8**, eabl9927 (2022).
- [14] D. F. Segedin, B. H. Goodge, G. A. Pan, Q. Song, H. LaBollita, M.- C. Jung, H. El-Sherif, S. Doyle, A. Turkiewicz, N. K. Taylor, J. A. Mason, A. T. N'Diaye, H. Paik, I. El Baggari, A. S. Botana, L. F. Kourkoutis, C. M. Brooks, and J. A. Mundy, *Nat. Commun.* **14**, 1468 (2023).
- [15] Q. Li, C. He, J. Si, X. Zhu, Y. Zhang, and H.- H. Wen, *Commun. Mater.* **1**, 16 (2020).
- [16] P. Puphal, Y.- M. Wu, K. Fürsich, H. Lee, M. Pakdaman, J. A. N. Bruin, J. Nuss, Y. E. Suyolcu, P. A. van Aken, B. Keimer, M. Isobe, and M. Hepting, *Sci. Adv.* **7**, eabl8091 (2021).
- [17] L. Wang, K. A. Stoerzinger, L. Chang, J. Zhao, Y. Li, C. S. Tang, X. Yin, M. E. Bowden, Z. Yang, H. Guo, L. You, R. Guo, J. Wang, K. Ibrahim, J. Chen, A. Rusydi, J. Wang, S. A. Chambers, and Y. Du, *Adv. Funct. Mater.* **28**, 1803712 (2018).
- [18] J. G. Lee, J. Hwang, H. J. Hwang, O. S. Jeon, J. Jang, O. Kwon, Y. Lee, B. Han, and Y.- G. Shul, *J. Am. Chem. Soc.* **138**, 3541 (2016).
- [19] N. Li, D. K. Bediako, R. G. Hadt, D. Hayes, T. J. Kempa, F. von Cube, D. C. Bell, L. X. Chen, and D. G. Nocera, *Proc. Natl. Acad. Sci. USA* **114**, 1486 (2017).
- [20] B. Weng, Z. Song, R. Zhu, Q. Yan, Q. Sun, C. G. Grice, Y. Yan, and W.- J. Yin, *Nat. Commun.* **11**, 3513 (2020).
- [21] J. Zaanen, G. A. Sawatzky, and J. W. Allen, *Phys. Rev. Lett.* **55**, 418 (1985).
- [22] K. Lee, B. H. Goodge, D. Li, M. Osada, B. Y. Wang, Y. Cui, L. F. Kourkoutis, and H. Y. Hwang, *APL Mater.* **8**, 041107 (2020).
- [23] J. Liu, E. Jia, L. Wang, K. A. Stoerzinger, H. Zhou, C. S. Tang, X. Yin, X. He, E. Bousquet, M. E. Bowden, A. T. S. Wee, S. A. Chambers, and Y. Du, *Adv. Sci.* **6**, 1901073 (2019).
- [24] S. Zeng, C. S. Tang, X. Yin, C. Li, M. Li, Z. Huang, J. Hu, W. Liu, G. J. Omar, H. Jani, Z. S. Lim, K. Han, D. Wan, P. Yang, S. J. Pennycook, A. T. S. Wee, and A. Ariando, *Phys. Rev. Lett.* **125**, 147003 (2020).
- [25] Y. Li, W. Sun, J. Yang, X. Cai, W. Guo, Z. Gu, Y. Zhu, and Y. Nie, *Front. Phys.* **9**, 719534 (2021).
- [26] L. Wang, Z. Yang, X. Yin, S. D. Taylor, X. He, C. S. Tang, M. E. Bowden, J. Zhao, J. Wang, J. Liu, D. E. Perea, L. Wangoh, A. T. S. Wee, H. Zhou, S. A. Chambers, and Y. Du, *Sci. Adv.* **7**, eabe2866 (2021).
- [27] L. Wang, Z. Yang, M. E. Bowden, J. W. Freeland, P. V. Sushko, S. R. Spurgeon, B. Matthews, W. S. Samarakoon, H. Zhou, Z. Feng, M. H. Engelhard, Y. Du, and S. A. Chambers, *Adv. Mater.* **32**, 2005003 (2020).
- [48] G. Kresse and J. Furthmüller, *Phys. Rev. B* **54**, 11169 (1996).
- [28] L. Wang, J. Zhao, C.- T. Kuo, B. E. Matthews, M. T. Oostrom, S. R. Spurgeon, Z. Yang, M. E. Bowden, L. W. Wangoh, S.- J. Lee, J.- S. Lee, E.- J. Guo, J. Wang, S. A. Chambers, and Y. Du, *Phys. Rev. Mater.* **6**, 075006 (2022).
- [29] E. Cho, K. Klyukin, S. Ning, J. Li, R. Comin, R. J. Green, B. Yildiz, and C. A. Ross, *Phys. Rev. Mater.* **5**, 094413 (2021).
- [30] F. Calle-Vallejo, J. I. Martínez, J. M. García-Lastra, M. Mogensen, and J. Rossmeisl, *Angew. Chem. Int. Ed.* **49**, 7699 (2010).
- [31] M. Zinkevich, *J. Solid State Chem.* **178**, 2818 (2005).

- [32] Y. Takeda, T. Hashino, H. Miyamoto, F. Kanamaru, S. Kume, and M. Koizumi, *J. Inorg. Nucl. Chem.* **34**, 1599 (1972).
- [33] R. Gottschall, R. Schöllhorn, M. Muhler, N. Jansen, D. Walcher, and P. Güttlich, *Inorg. Chem.* **37**, 1513 (1998).
- [34] J. J. Lander, *Acta Cryst.* **4**, 148 (1951).
- [35] A. M. Arévalo-López, M. Huvé, P. Simon, and O. Mentré, *Chem. Commun.* **55**, 3717 (2019).
- [36] M. Retuerto, F. Calle-Vallejo, L. Pascual, P. Ferrer, Á. García, J. Torrero, D. Gianolio, J. L. G. Fierro, M. A. Peña, J. A. Alonso, and S. Rojas, *J. Power Sources* **404**, 56 (2018).
- [37] J. G. Lee, H. J. Hwang, O. Kwon, O. S. Jeon, J. Jang, and Y.-G. Shul, *Chem. Commun.* **52**, 10731 (2016).
- [38] J. J. Lander and L. A. Wooten, *J. Am. Chem. Soc.* **73**, 2452 (1951).
- [39] A. Biswas, C.-H. Yang, R. Ramesh, and Y. H. Jeong, *Prog. Surf. Sci.* **92**, 117 (2017).
- [40] See Supplemental Material at <http://link.aps.org/supplemental/10.1103/PhysRevMaterials.7.085004> for the following details: experimental methods; Supplemental Material Fig. S1, RHEED patterns of the BNO thin film at different stages; Supplemental Material Fig. S2, *a*- and *c*-axes peaks simulations; Supplemental Material Fig. S3, hexagonal symmetry, X-ray Reflectivity (XRR) and RSM; Supplemental Material Fig. S4, STEM and EELS characterization of the interfacial transition region; Supplemental Material Fig. S5, simulated STEM-HAADF images; Supplemental Material Fig. S6, supercells used to examine the dependence of p-BNO and h-BNO stability; Supplemental Material Fig. S7, *in situ* nickel 3p XPS and *ex situ* nickel *K*-edge XAS; and Supplemental Material Fig. S8, NiO secondary phase captured by STEM, which includes Refs. [46–55].
- [41] P. C. Rogge, R. U. Chandrasena, A. Cammarata, R. J. Green, P. Shafer, B. M. Lefler, A. Huon, A. Arab, E. Arenholz, H. N. Lee, T.-L. Lee, S. Nemšák, J. M. Rondinelli, A. X. Gray, and S. J. May, *Phys. Rev. Mater.* **2**, 015002 (2018).
- [42] L. Wang, Y. Du, P. V. Sushko, M. E. Bowden, K. A. Stoerzinger, S. M. Heald, M. D. Scafetta, T. C. Kaspar, and S. A. Chambers, *Phys. Rev. Mater.* **3**, 025401 (2019).
- [43] R. Qiao, L. A. Wray, J.-H. Kim, N. P. W. Pieczonka, S. J. Harris, and W. Yang, *J. Phys. Chem. C* **119**, 27228 (2015).
- [44] G. Greczynski and L. Hultman, *J. Appl. Phys.* **132**, 011101 (2022).
- [45] W.-S. Yoon, M. Balasubramanian, K. Y. Chung, X.-Q. Yang, J. McBreen, C. P. Grey, and D. A. Fischer, *J. Am. Chem. Soc.* **127**, 17479 (2005).
- [46] S. Roychoudhury, R. Qiao, Z. Zhuo, Q. Li, Y. Lyu, J. Kim, J. Liu, E. Lee, B. J. Polzin, J. Guo, S. Yan, Y. Hu, H. Li, D. Prendergast, and W. Yang, *Energy Environ. Mater.* **4**, 246 (2021).
- [47] C. T. Koch, Ph.D. dissertation, Determination of core structure periodicity and point defect density along dislocations, Arizona State University, Phoenix, 2002.
- [49] J. P. Perdew, A. Ruzsinszky, G. I. Csonka, O. A. Vydrov, G. E. Scuseria, L. A. Constantin, X. Zhou, and K. Burke, *Phys. Rev. Lett.* **100**, 136406 (2008).
- [50] P. E. Blöchl, *Phys. Rev. B* **50**, 17953 (1994).
- [51] D. A. Muller, N. Nakagawa, A. Ohtomo, J. L. Grazul, and H. Y. Hwang, *Nature (London)* **430**, 657 (2004).
- [52] D. Guan, J. Zhong, H. Xu, Y.-C. Huang, Z. Hu, B. Chen, Y. Zhang, M. Ni, X. Xu, W. Zhou, and Z. Shao, *Appl. Phys. Rev.* **9**, 011422 (2022).
- [53] H. Zhang *et al.*, *Adv. Funct. Mater.* **32**, 2207618 (2022).
- [54] P. Adiga, L. Wang, C. Wong, B. E. Matthews, M. E. Bowden, S. R. Spurgeon, G. E. Sterbinsky, M. Blum, M.-J. Choi, J. Tao, T. C. Kaspar, S. A. Chambers, K. A. Stoerzinger, and Y. Du, *Nanoscale* **15**, 1119 (2023).
- [55] D. Guan, K. Zhang, Z. Hu, X. Wu, J. Chen, C. Pao, Y. Guo, W. Zhou, and Z. Shao, *Adv. Mater.* **33**, 2103392 (2021).